

A cryogenic scattering-type scanning near-field optical microscope

Honghua U. Yang,^{a)} Erik Hebestreit,^{a)} Erik E. Josberger,^{b)} and Markus B. Raschke^{c)}

Department of Physics, Department of Chemistry, and JILA, University of Colorado, Boulder, Colorado 80309, USA

(Received 24 October 2012; accepted 11 January 2013; published online 1 February 2013)

Scattering-type scanning near-field optical microscopy (*s*-SNOM) provides few nanometer optical spatial resolution and is compatible with nearly any form of linear and nonlinear optical spectroscopy. We have developed a versatile *s*-SNOM instrument operating under cryogenic and variable temperature (~ 20 –500 K) and compatible with high magnetic fields (up to 7 T). The instrument features independent tip and sample scanning and free-space light delivery with an integrated off-axis parabolic mirror for tip-illumination and signal collection with a numerical aperture of $N.A. = 0.45$. The optics operate from the UV to THz range allowing for continuous wave, broadband, and ultrafast *s*-SNOM spectroscopy, including different variants of tip-enhanced spectroscopy. We discuss the instrument design, implementation, and demonstrate its performance with mid-infrared Drude response *s*-SNOM probing of the domain formation associated with the metal-insulator transitions of VO_2 ($T_{MIT} \simeq 340$ K) and V_2O_3 ($T_{MIT} \simeq 150$ K). This instrument enables the study of mesoscopic order and domains of competing quantum phases in correlated electron materials over a wide range of controlled electric and magnetic fields, strain, current, and temperature. © 2013 American Institute of Physics. [<http://dx.doi.org/10.1063/1.4789428>]

I. INTRODUCTION

Strong electron correlations in transition metal oxides and related materials can lead to unusually rich phase diagrams with distinct crystallographic, electronic, and magnetic phases, often with frustration and degenerate ground states. In many cases the strong electron, spin, and lattice interactions result in phase competition and coexistence of multiple phases near the phase boundaries.^{1,2}

The origins of these spatial phase inhomogeneities, especially in nominally homogeneous pure single crystals, has been an intensely debated issue in condensed matter physics.^{1–6} The problem is difficult to track theoretically, as the role of domains in defining macroscopic material properties is often unclear. In addition, despite some notable exceptions, most experimental evidence of spatial phase inhomogeneity is indirect due to a lack of versatile imaging techniques with the necessary spatial resolution, that are applicable *in situ*, ideally under variable magnetic and electric fields, and that are simultaneously sensitive to the different relevant order parameters.^{7,8}

Evidence of local phase separation and domain formation on mesoscopic length scales is often indirect from bulk measurements of electronic transport,^{9,10} X-ray and neutron diffraction,^{11,12} and angle-resolved photo-emission spectroscopy.¹³ Here, macroscopic quantities, which are expected to exhibit a discontinuous change at the phase transition temperature are instead found to be broadened due to the formation of an inhomogeneous phase distribution of *a priori* unknown texture and domain sizes.

In an effort to gain information about the underlying domain structure and its spatial evolution during phase transitions of correlated electron materials, scanning tunneling microscopy,^{14–19} electron microscopy techniques,^{20–24} photoelectron emission microscopy (PEEM),²⁵ magnetic force microscopy,^{26–29} piezoresponse force microscopy,³⁰ conductive atomic force microscopy (AFM),^{6,31} and others have been applied with great success. Although powerful, these techniques often cannot image multiple order parameters simultaneously. Moreover, these techniques are generally not compatible with large external magnetic or electric fields.

Optical techniques could overcome these limitations. With relevant energy scales defined by electronic and lattice excitations, optical imaging and spectroscopy at meV to eV energies provide direct contrast between, and simultaneous insight into the structural changes of the material which are characteristic of the different phases. In addition, optical spectroscopy is compatible with a wide range of internal and external stimuli including strain, electric fields, and magnetic fields. While the spatial resolution is in general diffraction limited in the far-field, by combining optical spectroscopy with scanning probe microscopy we can achieve nanoscale optical resolution in the near-field, through as scattering-type scanning near-field optical microscopy (*s*-SNOM).

The imaging contrast is provided by the optical field localization at the nanoscale tip apex and its optical antenna properties. The tip (generally 5–20 nm radius of curvature) acts as a local scattering source for the enhanced evanescent optical fields localized between the AFM tip and the sample surface. The scattered light from the tip-apex region then contains spectroscopic information about the sample from a region confined laterally by the dimensions of the tip apex radius.

The *s*-SNOM signal reflects the near-surface bulk properties of a sample to a depth on the order of several nm, as given

^{a)}H. U. Yang and E. Hebestreit contributed equally to this work.

^{b)}Current address: Department of Electrical Engineering, University of Washington, Seattle, Washington 98195, USA.

^{c)}Electronic mail: markus.raschke@colorado.edu.

by the spatial extent of evanescent field of the tip apex. The signal is thus largely insensitive to surface electronic states and surface contaminants.

s-SNOM can be applied over a wide wavelength range, from the UV up to the THz regime. The signal is generated by a scattering mechanism which relies solely on free space excitation and detection and is therefore intrinsically broadband and compatible with ultrafast laser spectroscopy. This is in contrast to fiber based near-field scanning optical microscopy (NSOM)^{32,33} which is limited in spatial resolution, sensitivity, and usable wavelength range, by aperture transmission, waveguide cut-off, and fiber material.

s-SNOM, as a purely optical technique, is compatible with variable and cryogenic temperatures, as well as large magnetic and electric fields. The local optical near-field interaction in *s*-SNOM can couple directly to electronic and vibrational resonances, spin order, lattice symmetry, and therefore provides contrast due to many mechanisms including the metallic infrared Drude response, nanoscale impedance, infrared and Raman vibrational response, or non-linear optical interactions.

With the appropriate choice and combination of those techniques, multiple order parameters can be probed simultaneously in real space. These unique nanoscale spectroscopic capabilities make *s*-SNOM a versatile tool for the spectroscopic imaging of as yet poorly understood material systems, such as correlated electron systems.

Currently, investigations of correlated electron materials using *s*-SNOM have been carried out at or above room temperature,^{34,35} and only a limited number of specialized low temperature *s*-SNOM systems have been developed.^{36–39} All currently reported designs have either small numerical apertures, operate in transmission mode, are not capable of operating under large magnetic fields, or are not generally compatible with a broad range of optical techniques including ultrafast laser pulses.^{36–39} Although many low tempera-

ture NSOM designs exist,^{40–48} the requirements for a low-temperature *s*-SNOM system are quite different.

In this paper, we report on the development of a versatile *s*-SNOM system, operating at temperatures from 500 K down below 20 K, over a broad spectral range from the UV to mid-infrared, and compatibility with a superconducting multi-Tesla magnet.

II. INSTRUMENT DESIGN

The design of our cryogenic *s*-SNOM instrument requires a set of primary considerations critical for reaching the desired optical, thermal, and magnetic field specifications. The overall geometry of the setup is determined by the need for broadband illumination, large solid angle for tip-scattered light collection, compatibility with low temperatures, and large magnetic fields. This leads to several trade-offs, e.g., a compact design is desired to fit into the bore of a superconducting magnet which restricts the optical access with large numerical aperture for most efficient apex illumination and near-field scattering collection.

Given the restricted space inside the magnet bore, the incident and outgoing beams are chosen to be parallel or collinear. Furthermore, the incident beam enters the apparatus from the bottom, such that the optical axis is parallel to the magnetic flux lines and instrument axis (Fig. 1). This illumination scheme requires only a single-solenoid magnet, while simultaneously yielding a short and interferometrically stable beam delivery. This design also allows to maintain the conventional upright AFM orientation.

An off-axis parabolic mirror is positioned at the side of the sample stage with its focus at the tip location. The numerical aperture is maximized within the limits set by the sample plane, tip axis, scan range, magnet geometry, and beam size. Independent tip and sample positioning is desirable for an optimal optical alignment procedure as discussed in Sec. II B.

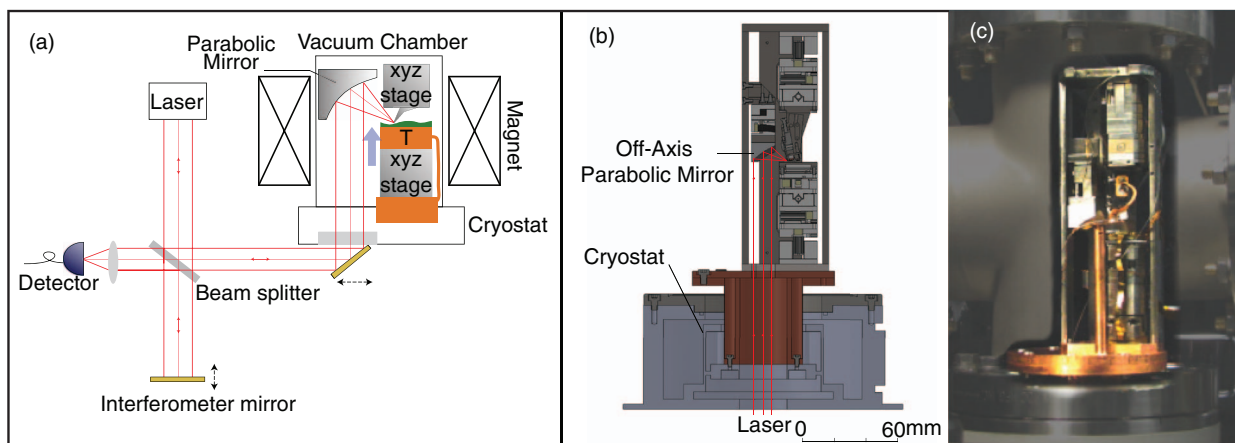


FIG. 1. Cryogenic scattering-type scanning near-field optical microscopy (*s*-SNOM) system, based on a contact and dynamic force AFM with parabolic optics for tip illumination and collection of scattered near-field light. (a) *s*-SNOM schematic. The arrow in the center of the vacuum chamber indicates the magnetic field direction; the copper block marked with T is the heater and temperature sensor connected to the flow cryostat. (b) Cross-sectional view of core components. The AFM consists of two positioners for independent tip and sample spatial control. Light is focused by an off-axis parabolic mirror, mounted on a 2-axis goniometer. All components are held by a titanium housing mounted on a continuous flow cryostat, with optical access through its base for epi-illumination and detection. The dimensions are minimized such that insertion into a high-field superconducting magnet (not shown) is possible. (c) Photo of the *s*-SNOM apparatus, with AFM inside the test chamber (cut away view).

Cooling is performed by a modified Janis ST500 cryostat. It features an exchangeable 25 mm diameter bottom window, e.g., BaF₂ (ISP-Optics, BF-W-38-5) used for the experiments demonstrated here, and suitable for experiments from the UV to mid-IR. The cryostat was chosen to meet the temperature requirements. All materials inside the chamber are chosen to be high-vacuum compatible. With a turbo-molecular pump (Pfeiffer HiCube Eco pump station) a pressure $<10^{-5}$ mbar is reached at room temperature.

A. AFM

A dynamic force AFM (Attocube Systems AG) serves as the core component for the cryogenic *s*-SNOM system. It consists of two 3-axis piezo slip-stick stages (ANPxyz101) for independent tip and sample positioning. Each stage features a 5 mm coarse xyz travel range, with a step size of about 100 nm at room temperature.

An open loop 3-axis piezo scanner (ANSxyz100) is mounted on top of the sample stage. This scanner has a range of $50\ \mu\text{m} \times 50\ \mu\text{m} \times 24\ \mu\text{m}$ at room temperature ($30\ \mu\text{m} \times 30\ \mu\text{m} \times 15\ \mu\text{m}$ at 4 K). The cantilever oscillation is tracked interferometrically by a single mode fiber placed 50–100 μm from the backside of the cantilever.⁴⁹ The AFM allows for a variety of imaging modes, including conductive, magnetic force, contact and non-contact atomic force microscopy.

A titanium housing for the components ensures a non-magnetic, rigid mounting with low vibration transmission. The translation stages are also made of titanium, and provide minimal absolute and relative thermal expansion. The slender design of the positioners and scanners with outer dimension of $\sim 24\ \text{mm} \times 24\ \text{mm}$ leaves enough space for the free space optical beam delivery and provides for a good fit into a typical 75 mm diameter superconducting magnet bore.

The vibration spectrum was analyzed with both an external accelerometer and a built-in AFM noise analyzer. Results indicated minimal vibrations levels, with mechanical amplitudes $\lesssim 1\ \text{nm}$ (root-mean-square).

B. Optics

Free space beam delivery of the incident and scattered beams is necessary for *s*-SNOM in order to allow for a wide spectral range (UV–THz), and large spectral bandwidth, also desired for short pulse excitations. This rules out fiber delivery due to dispersion and transmission constraints.

For broadband light and ultrashort laser pulse illumination, reflective optics are superior to refractive optics since the absence of material dispersion eliminates any chromatic or other aberration for confocal applications. Parabolic mirrors are preferable to Cassegrain objectives, as they are more compact and have shorter focal lengths. However, parallelism of the incident light beam with respect to the optical axis of the off-axis parabolic mirror is crucial to avoid coma in the focus.^{50,51}

Based on an empirical function fitted to simulated data,⁵¹ we estimate that a tilt of δ from the parabolic mirror axis would reduce the peak intensity to $1.26 \times e^{-290\delta/\lambda}$ for δ be-

tween 0.02° to 0.07° (λ in μm). Even a tilt of 0.03° would already strongly deform the focus, and although the FWHM of the center peak only increases by a few percent, the peak intensity is reduced by a factor of two, e.g., for 10 μm wavelength light.

A customized off-axis parabolic mirror (Nu-Tek Precision Optical Corporation) with a focal length of 11.25 mm and a numerical aperture of 0.45 is used. The surface roughness is specified to be 7 nm RMS and the form accuracy is specified to be below $0.625\ \mu\text{m}$. The mirror is mounted on a piezo-driven 2-axis goniometer (Attocube ANGt50/ANGp50) with a tilting resolution of 10^{-4} degree. With the aid of a flat face precision machined on the mirror, the mirror axis is aligned to the incident visible alignment laser beam.⁵² Fine tuning of the laser focus is achieved by imaging the tip onto a CCD camera and optimizing the tip apex scattering to be as small and symmetric as possible. Different laser sources can then readily be coupled into the system by aligning them co-linearly with the alignment laser.

C. Cryostat and vacuum system

A number of factors are taken into account for optimal sample cooling. A thermal link made of a stack of 20 laser welded gold plated Oxygen-free high thermal conductivity (OFHC) copper foils (Attocube Systems AG, ATC100), with thermal conductivity of 10 mW/K is used to couple the sample to the cryostat.

To minimize the heat conduction from the translation stage to the sample holder, a teflon thermal isolation plate sandwiched by two layers of aluminized mylar foil is placed underneath the sample holder. The multiple interfaces between sample holder and the translation stage reduce the heat conductance to be below 1 mW/K.⁵³

To minimize heating effects through heat conduction via the wires of the heater and the temperature sensor, these cables were coiled around the cryostat and pre-cooled. Finally, to keep laser heating of the sample at a minimum, the incident laser power should be kept below 10 mW, which is a typical power level for *s*-SNOM.

The heat conduction via the gas with pressure below 0.1 Pa is estimated from $\dot{q}_{\text{gas}} = 0.5kpA\Delta T$, where k is an empirical coefficient of 1.2 for air, p the pressure (Pa), A the sample holder surface area (m^2), and ΔT the temperature difference between sample and the room temperature chamber wall (K).⁵³ For our conditions \dot{q}_{gas} can be estimated to be $\sim 0.7\ \text{mW}$, and is therefore negligible.

A significant heat load arises from radiant heat flow from the surrounding chamber walls at 300 K to the sample holder at, e.g., 80 K when cooled with liquid nitrogen. We can estimate the heat transfer using the black-body radiation expression $\dot{q}_{\text{rad}} = \sigma EA(T_{\text{Env}}^4 - T_{\text{Samp}}^4)$, to be $\sim 130\ \text{mW}$, with σ the Stefan-Boltzmann constant, E a factor related to the emissivities of the surfaces (taken as 0.5), A the sample holder surface area (m^2), and T_{Env} and T_{Samp} the environment and sample temperature, respectively. A thin copper radiation shield was built around the AFM and linked to the cryostat to reduce the thermal radiation. With the radiation shield at $\approx 100\ \text{K}$ the radiation power is reduced to $<1\ \text{mW}$ for N₂ (I) cooling.

Based on the above analysis, we estimate a 30 mW cooling power necessary for maintaining the sample at 80 K. The sample temperature is controlled with a resistive heater and a temperature controller (Cryocon 32B), with a maximum power of 5 W, and stability within ± 0.1 K.

D. Magnet

In the design, a multi-filamentary niobium-titanium superconducting magnet (Janis 6.5 T-74) was used as a representative model. This superconducting magnet can produce a 6.5 T vertical field, with a moderate inhomogeneity of $\pm 0.5\%$ over a 1 cm sphere. Within a typical AFM scan area of $10 \mu\text{m} \times 10 \mu\text{m}$, the inhomogeneity is below $10^{-3}\%$. The vertical center bore has a diameter of 74 mm. All the piezo motors, including goniometers, coarse positioners, and scanners, are made of titanium and have demonstrated functionality under 7 T magnetic fields (specified up to 31 T).

III. CHARACTERIZATION/RESULTS AND DISCUSSION

A. Near-field contrast of gold on silicon reference sample

To test the general system performance we perform elastic IR *s*-SNOM with contrast resulting from the metallic Drude response. Light from a CO₂ laser (*p*-polarized, $I = 5$ mW, $\lambda = 10.6 \mu\text{m}$) is focused onto a commercial Pt-Ir coated AFM tip (Nanosensors, Arrow NCpt). The optical signal is detected in the back scattered direction by a liquid nitrogen cooled HgCdTe detector (Judson, J15D14-M204-S250U-30) with a high bandwidth transimpedance preamplifier (Femto, HVA-S).

The AFM operates in dynamic force mode, with a controlled tip oscillation amplitude of about 20 nm, and frequency $\Omega \approx 250$ kHz. The near-field contribution is selected by lock-in demodulation at harmonics of the tip oscillation frequency (Ω , 2Ω , and 3Ω). The optical response during approach gives a clear indication of the near-field optical contrast.⁵⁴ Approach curves over the flat gold section in Figure 2(a) show a strong nonlinear distance dependence, confirming the near-field signal origin.

Interferometric signal amplification and detection conveniently provides both near-field amplitude and phase by modulating the phase of the reference field E_{ref} at a frequency ω_{ref} (Fig. 1(a)).⁵⁵ The signal at the detector contains a near-field component E_{NF} , far-field background from the tip shaft and sample surface E_{bg} , and the reference field E_{ref} , with total intensity $I \propto |E_{\text{sig}}(\Omega) + E_{\text{bg}}(\Omega) + E_{\text{ref}}(\omega_{\text{ref}})|^2$. The near-field E_{NF} is extracted by demodulating I at side bands of frequency $n\Omega + m\omega_{\text{ref}}$, where n, m are integers.⁵⁶ Figures 2(b)–2(d) show an *s*-SNOM scan demodulated at 2Ω sideband across the edge of a Au film evaporated onto a silicon surface. The simultaneously acquired topographic and *s*-SNOM images demonstrate the optical dielectric contrast between gold and silicon in the optical amplitude. The signal variation directly along the Si-Au edge is a topographic artifact.⁵⁷ No obvious phase contrast is expected and the small variation of $\Delta\phi \sim 10^\circ$ observed (Fig. 2(d)) is due to residual far-field interference.

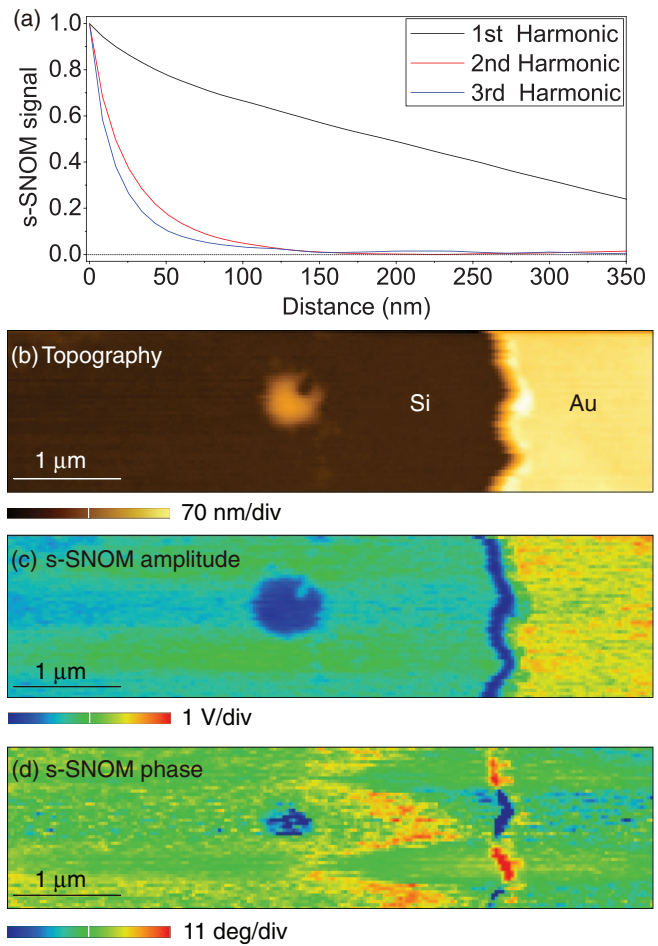


FIG. 2. *s*-SNOM approach curves on a Au surface at the first three tip harmonic demodulations show a near-field localization < 30 nm (a). Panels (b)–(d) display the topography and associated *s*-SNOM optical signal for a Au-Si interface using optical excitation from a CO₂ laser ($\lambda = 10.6 \mu\text{m}$). An optical dielectric material contrast is observed in near-field amplitude (c), but only negligible in phase (d) due to the non-resonant properties of Au and Si/SiO₂ at the excitation wavelength.

B. Image of phase transition of VO₂ and V₂O₃

To demonstrate the ability to probe phase transitions above and below room temperature, micrometer-sized vanadium dioxide (VO₂) single crystals on a silicon substrate were imaged. VO₂ undergoes a first-order metal-insulator transition (MIT) from a low-temperature monoclinic insulating phase to a high-temperature rutile (R) metallic phase at $T_{\text{MIT}} = 340$ K. These substrate bounded single crystals form domains during the MIT due to external substrate-induced stress.³⁴ Figure 3 shows the *s*-SNOM image with corresponding topography. The crystal remains insulating at 340 K (Fig. 3(b)) and becomes metallic at 355 K (Fig. 3(d)) with contrast due to the increase in optical conductivity of the metallic phase. *s*-SNOM line scan over a VO₂ crystal (Fig. 3(e)) shows optical contrast of metallic domains, with no topographic variation.

V₂O₃ is a paramagnetic metal at room temperature with a MIT around 150 K, accompanied by a structural change from rhombohedral to monoclinic symmetry.⁵⁸ It

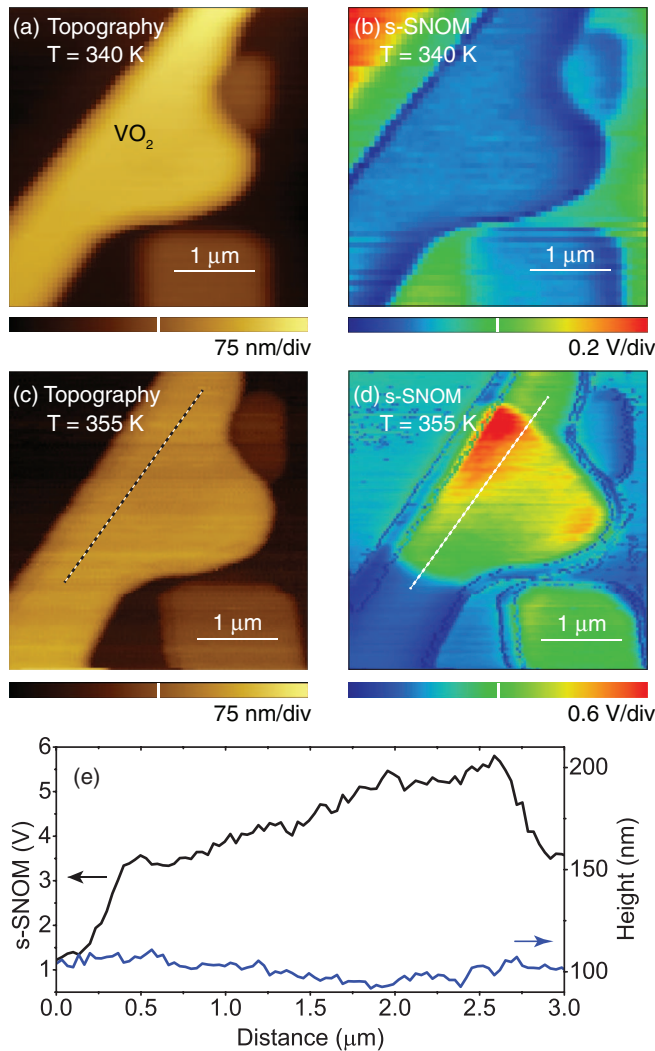


FIG. 3. The topography (a), (c) and near-field response taken with a CO₂ laser at 10.6 μm (b), (d) of a VO₂ crystal at 340 K (a), (b) and 355 K (c), (d). Due to the difference in optical conductivity between the metallic and insulating phases, the insulating phase appears dark and the metallic phase appears bright. (e) *s*-SNOM signal together with topography line-scan along the dashed line in (c), (d).

undergoes magnetic ordering from a paramagnetic metal to an antiferromagnetic insulator.⁵⁹ The MIT can be tuned by pressure or doping which modifies the magnetic ordering. Recently, the domain evolution across the paramagnetic insulator to paramagnetic metal phase transition on chromium doped V₂O₃ ((V_{1-x}Cr_x)₂O₃, $x = 0.011$) was studied using PEEM.⁶⁰ Here we use micrometer sized V₂O₃ single crystals to demonstrate the *s*-SNOM system performance at low temperature. The sample has been pre-characterized by cryogenic Raman measurement, and the phase transition manifests itself in phonon Raman response acquired *ex situ* at different temperatures as shown in Fig. 4(a). A corresponding *s*-SNOM image is shown in Fig. 4(c). Upon cooling, at temperatures ~200 K, the emergence of insulating domains is observed. They appear to nucleate around topographic defects, with domain topology similar to what has been observed before.⁶⁰

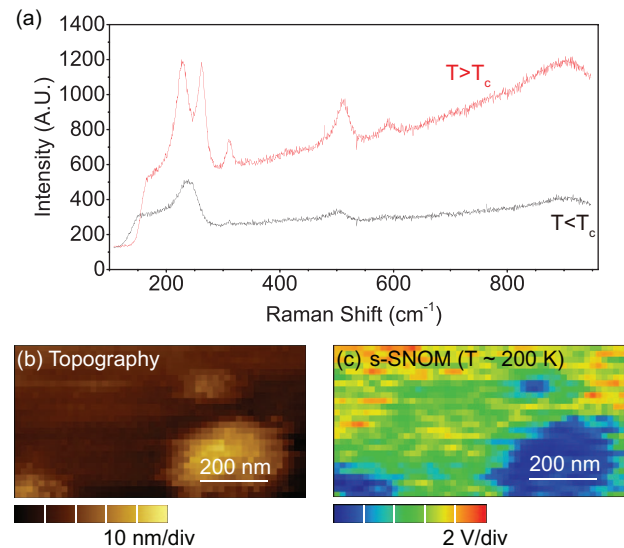


FIG. 4. Cryogenic micro-Raman (a), and mid-IR *s*-SNOM images of doped V₂O₃ (taken with a CO₂ laser at 10.6 μm) (c) with corresponding topography (b). Metallic phases (red) with spatial variation on 10's nm are seen to nucleate near defects (large islands are a dielectric surface impurity).

IV. CONCLUSION/OUTLOOK

In conclusion, we have developed a versatile cryogenic *s*-SNOM system compatible with strong magnetic fields for multimodal and multispectral imaging. This system, in combination with linear, nonlinear, and ultrafast spectroscopy, could provide spectroscopic access to electronic and vibrational resonances, structural symmetry, and femtosecond dynamics with few-nanometer spatial resolution.⁶¹ The sensitivity, specificity, and selectivity of the optical interaction allows for the systematic real space probing of multiple order parameters and phases of complex materials simultaneously. The tool is applicable to a wide range of materials with related physical phenomena, including organic conductors and semiconductors which also exhibit electron correlation, charge order, and superconducting gaps.

ACKNOWLEDGMENTS

We gratefully acknowledge technical support from Christoph Bödefeld, Reinhold Pohlner, Christian Mitzkus, and Martin Zech (Attocube Systems, AG). This work is dedicated to Carsten Georgi, who passed away in a tragic accident shortly after joining the development team. We also thank Andrew Jones for help with the *s*-SNOM measurements. VO₂ and V₂O₃ samples were kindly provided by David Cobden, University of Washington. The work has been supported by the Department of Energy, Division of Materials Sciences and Engineering (Grant No. DE-SC0002197). E.H. acknowledges the DAAD RISE program.

¹E. Dagotto, *Science* **309**, 257 (2005).

²N. Mathur and P. Littlewood, *Solid State Commun.* **119**, 271 (2001).

³A. Moreo, S. Yunoki, and E. Dagotto, *Science* **283**, 2034 (1999).

⁴E. Dagotto, T. Hotta, and A. Moreo, *Phys. Rep.* **344**, 1 (2001).

⁵M. Fiebig, T. Lottermoser, D. Fröhlich, A. V. Goltsev, and R. V. Pisarev, *Nature (London)* **419**, 818 (2002).

- ⁶T. Choi, Y. Horibe, H. T. Yi, Y. J. Choi, W. Wu, and S.-W. Cheong, *Nature Mater.* **9**, 253 (2010).
- ⁷V. B. Shenoy, D. D. Sarma, and C. N. R. Rao, *ChemPhysChem* **7**, 2053 (2006).
- ⁸V. B. Shenoy and C. Rao, *Philos. Trans. R. Soc. London, Ser. A* **366**, 63 (2008).
- ⁹Y. Tokunaga, M. Tokunaga, and T. Tamegai, *Phys. Rev. B* **71**, 012408 (2005).
- ¹⁰T. Z. Ward, Z. Gai, H. W. Guo, L. F. Yin, and J. Shen, *Phys. Rev. B* **83**, 125125 (2011).
- ¹¹P. M. Woodward, D. E. Cox, T. Vogt, C. N. R. Rao, and A. K. Cheetham, *Chem. Mater.* **11**, 3528 (1999).
- ¹²C. Ritter, R. Mahendiran, M. R. Ibarra, L. Morellon, A. Maignan, B. Raveau, and C. N. R. Rao, *Phys. Rev. B* **61**, R9229 (2000).
- ¹³Z. Sun, J. F. Douglas, A. V. Fedorov, Y.-D. Chuang, H. Zheng, J. F. Mitchell, and D. S. Dessau, *Nat. Phys.* **3**, 248 (2007).
- ¹⁴M. Fath, "Scanning tunneling spectroscopy on correlated electron systems," Ph.D. dissertation (Universiteit Leiden, 1999).
- ¹⁵S. H. Pan, J. P. O'Neal, R. L. Badzey, C. Chamon, H. Ding, J. R. Engelbrecht, Z. Wang, H. Eisaki, S. Uchida, A. K. Gupta, K. W. Ng, E. W. Hudson, K. M. Lang, and J. C. Davis, *Nature (London)* **413**, 282 (2001).
- ¹⁶C. Renner, G. Aeppli, B. G. Kim, Y.-A. Soh, and S. W. Cheong, *Nature (London)* **416**, 518 (2002).
- ¹⁷K. McElroy, J. Lee, J. A. Slezak, D.-H. Lee, H. Eisaki, S. Uchida, and J. C. Davis, *Science* **309**, 1048 (2005).
- ¹⁸C. V. Parker, P. Aynajian, E. H. da Silva Neto, A. Pushp, S. Ono, J. Wen, Z. Xu, G. Gu, and A. Yazdani, *Nature (London)* **468**, 677 (2010).
- ¹⁹A. Meszaros, K. Fujita, H. Eisaki, S. Uchida, J. C. Davis, S. Sachdev, J. Zaanen, M. J. Lawler, and E. A. Kim, *Science* **333**, 426 (2011).
- ²⁰M. Uehara, S. Mori, C. H. Chen, and S. W. Cheong, *Nature (London)* **399**, 560 (1999).
- ²¹J. Xu, Y. Matsui, T. Kimura, and Y. Tokura, *Physica C* **357–360**, 401 (2001).
- ²²T. Asaka, S. Yamada, S. Tsutsumi, C. Tsuruta, K. Kimoto, T. Arima, and Y. Matsui, *Phys. Rev. Lett.* **88**, 097201 (2002).
- ²³J. C. Loudon, N. D. Mathur, and P. A. Midgley, *Nature (London)* **420**, 797 (2002).
- ²⁴J. Tao, D. Niebieskikwiat, M. Varela, W. Luo, M. A. Schofield, Y. Zhu, M. B. Salamon, J. M. Zuo, S. T. Pantelides, and S. J. Pennycook, *Phys. Rev. Lett.* **103**, 097202 (2009).
- ²⁵T. Taniuchi, H. Kumigashira, M. Oshima, T. Wakita, T. Yokoya, M. Kubota, K. Ono, H. Akinaga, M. Lippmaa, M. Kawasaki, and H. Koinuma, *Appl. Phys. Lett.* **89**, 112505 (2006).
- ²⁶L. Zhang, C. Israel, A. Biswas, R. L. Greene, and A. de Lozanne, *Science* **298**, 805 (2002).
- ²⁷W. Wu, C. Israel, N. Hur, S. Park, S.-W. Cheong, and A. de Lozanne, *Nature Mater.* **5**, 881 (2006).
- ²⁸D. Serrate, P. Ferriani, Y. Yoshida, S.-W. Hla, M. Menzel, K. von Bergmann, S. Heinze, A. Kubetzka, and R. Wiesendanger, *Nat. Nanotechnol.* **5**, 350 (2010).
- ²⁹J. H. Lee, L. Fang, E. Vlahos, X. Ke, Y. W. Jung, L. F. Kourkoutis, J.-W. Kim, P. J. Ryan, T. Heeg, M. Roeckerath, V. Goian, M. Bernhagen, R. Uecker, P. C. Hammel, K. M. Rabe, S. Kamba, J. Schubert, J. W. Freeland, D. A. Muller, C. J. Fennie, P. Schiffer, V. Gopalan, E. Johnston-Halperin, and D. G. Schlom, *Nature (London)* **466**, 954 (2010).
- ³⁰E. B. Lochocki, S. Park, N. Lee, S. W. Cheong, and W. Wu, *Appl. Phys. Lett.* **99**, 232901 (2011).
- ³¹T.-M. Chuang and A. de Lozanne, *Rev. Sci. Instrum.* **78**, 053710 (2007).
- ³²E. H. Syngé, *Philos. Mag.* **6**, 356 (1928).
- ³³D. W. Pohl, W. Denk, and M. Lanz, *Appl. Phys. Lett.* **44**, 651 (1984).
- ³⁴A. C. Jones, S. Berweger, J. Wei, D. Cobden, and M. B. Raschke, *Nano Lett.* **10**, 1574 (2010).
- ³⁵M. M. Qazilbash, M. Brehm, B.-G. Chae, P.-C. Ho, G. O. Andreev, B.-J. Kim, S. J. Yun, A. V. Balatsky, M. B. Maple, F. Keilmann, H.-T. Kim, and D. N. Basov, *Science (N.Y.)* **318**, 1750 (2007).
- ³⁶K. Taniguchi and Y. Kanemitsu, *Jpn. J. Appl. Phys.* **44**, 575 (2005).
- ³⁷A. Kirihaara, S. Kono, A. Tomita, and K. Nakamura, *Opt. Rev.* **13**, 279 (2006).
- ³⁸G. Andreev, "Application of infrared nanooptics to ultrathin materials," Ph.D. dissertation (University of California, 2011).
- ³⁹I. C. Moldovan-Doyen, G. Xu, L. Greusard, G. Sevin, E. Strupiechonski, G. Beaudoin, I. Sagnes, S. P. Khanna, E. H. Linfield, A. G. Davies, R. Colombelli, and Y. De Wilde, *Appl. Phys. Lett.* **98**, 231112 (2011).
- ⁴⁰R. D. Grober, T. D. Harris, J. K. Trautman, and E. Betzig, *Rev. Sci. Instrum.* **65**, 626 (1994).
- ⁴¹W. Göhde, J. Tittel, T. Basché, C. Bräuchle, U. C. Fischer, and H. Fuchs, *Rev. Sci. Instrum.* **68**, 2466 (1997).
- ⁴²G. Behme, A. Richter, M. Süptitz, and C. Lienau, *Rev. Sci. Instrum.* **68**, 3458 (1997).
- ⁴³S.-Y. Yim, J. S. Kim, Y. H. Kim, C. C. Byeon, O.-H. Cha, M. S. Jeong, D. J. Park, S. B. Choi, D. S. Kim, and C. Lienau, *J. Korean Phys. Soc.* **56**, 717 (2010).
- ⁴⁴Y. Durand, J. C. Woehl, B. Viellerobe, W. Göhde, and M. Orrit, *Rev. Sci. Instrum.* **70**, 1318 (1999).
- ⁴⁵M. H. Gray and J. W. P. Hsu, *Rev. Sci. Instrum.* **70**, 3355 (1999).
- ⁴⁶N. Fukutake, S. Takasaka, and T. Kobayashi, *J. Appl. Phys.* **91**, 849 (2002).
- ⁴⁷A. Bek, R. Vogelgesang, and K. Kern, *Rev. Sci. Instrum.* **77**, 043703 (2006).
- ⁴⁸E. Nazaretski, K. S. Graham, J. D. Thompson, J. A. Wright, D. V. Pelekhov, P. C. Hammel, and R. Movshovich, *Rev. Sci. Instrum.* **80**, 083704 (2009).
- ⁴⁹D. Rugar, H. J. Mamin, and P. Guethner, *Appl. Phys. Lett.* **55**, 2588 (1989).
- ⁵⁰M. Lieb and A. Meixner, *Opt. Express* **8**, 458 (2001).
- ⁵¹A. April, P. Bilodeau, and M. Piché, *Opt. Express* **19**, 9201 (2011).
- ⁵²Due to machining precision of about 1 mrad (0.057°), back-reflection is not sufficient to achieve the best alignment.
- ⁵³J. W. Ekin, *Experimental Techniques for Low-Temperature Measurements: Cryostat Design, Material Properties, and Superconductor Critical-Current Testing* (Oxford University Press, 2006).
- ⁵⁴M. B. Raschke and C. Lienau, *Appl. Phys. Lett.* **83**, 5089 (2003).
- ⁵⁵N. Ocelic, A. Huber, and R. Hillenbrand, *Appl. Phys. Lett.* **89**, 101124 (2006).
- ⁵⁶J. M. Atkin, S. Berweger, A. C. Jones, and M. B. Raschke, *Adv. Phys.* **61**, 745 (2012).
- ⁵⁷T. Taubner, R. Hillenbrand, and F. Keilmann, *J. Microsc.* **210**, 311 (2003).
- ⁵⁸P. Dernier and M. Marezio, *Phys. Rev. B* **2**, 3771 (1970).
- ⁵⁹D. McWhan, A. Jayaraman, J. Remeika, and T. Rice, *Phys. Rev. Lett.* **34**, 547 (1975).
- ⁶⁰S. Lupi, L. Baldassarre, B. Mansart, A. Perucchi, A. Barinov, P. Dudin, E. Papalazarou, F. Rodolakis, J. P. Rueff, J. P. Itié, S. Ravy, D. Nicoletti, P. Postorino, P. Hansmann, N. Parragh, A. Toschi, T. Saha-Dasgupta, O. K. Andersen, G. Sangiovanni, K. Held, and M. Marsi, *Nat. Commun.* **1**, 105 (2010).
- ⁶¹X. G. Xu, M. Rang, I. M. Craig, and M. B. Raschke, *J. Phys. Chem. Lett.* **3**, 1836 (2012).